Nanoscale

Accepted Manuscript

This article can be cited before page numbers have been issued, to do this please use: C. Tapeinos, A. Marino, M. Battaglini, S. Migliorin, R. Brescia, A. Scarpellini, M. Prato, F. Drago, C. de Julián Fernández and G. Ciofani, *Nanoscale*, 2018, DOI: 10.1039/C8NR05520C.

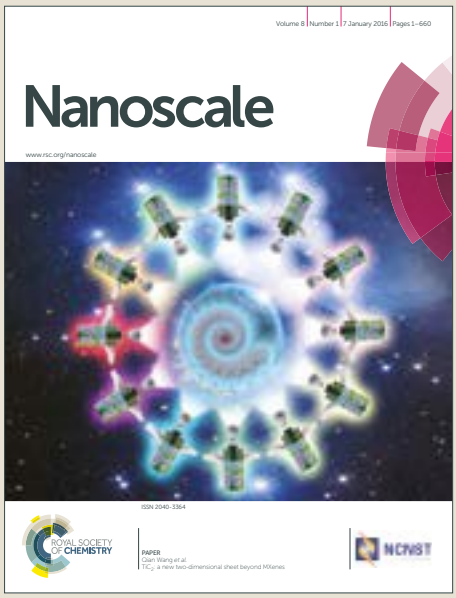

ROYAL SOCIETY OF CHEMISTRY

rsc.li/nanoscale

View Article Online
DOI: 10.1039/C8NR05520C

Stimuli-responsive lipid-based magnetic nanovectors increase apoptosis in glioblastoma cells through synergic intracellular hyperthermia and chemotherapy

Christos Tapeinos [a,†,], Attilio Marino [a,†,*], Matteo Battaglini [a,b], Simone Migliorin [c], Rosaria Brescia [d], Alice Scarpellini [d], César De Julián Fernández [e], Mirko Prato [f], Filippo Drago [g], Gianni Ciofani [a,c,*]*

[a] Smart Bio-Interfaces, Istituto Italiano di Tecnologia, Pontedera (Pisa), 56025 Italy

[b] The Biorobotics Institute, Scuola Superiore Sant'Anna, Pontedera (Pisa), 56025 Italy

[c] Department of Mechanical and Aerospace Engineering, Politecnico di Torino, Torino, 10129 Italy

[d] Electron Microscopy Facility, Istituto Italiano di Tecnologia, Genova, 16163 Italy

[e] Istituto dei Materiali per l'Elettronica e il Magnetismo, Consiglio Nazionale delle Ricerche - CNR, Parma, 43124 Italy.

[f] Materials Characterization Facility, Istituto Italiano di Tecnologia,Genova, 16163 Italy

[g] Nanochemistry Department, Istituto Italiano di Tecnologia, Genova, 16163 Italy

[†] These authors equally contributed to this work

[*] Corresponding authors

E-mail: christos.tapeinos@iit.it; attilio.marino@iit.it; gianni.ciofani@iit.it

View Article Online
DOI: 10.1039/C8NR05520C

Abstract

In this study, taking into consideration the limitations of the current treatments of glioblastoma multiforme, we fabricated a biomimetic lipid-based magnetic nanovector with good loading capacity and a sustained release profile of the encapsulated chemotherapeutic drug, temozolomide. These nanostructures demonstrated an enhanced release after exposure to an alternating magnetic field, and a complete release of the encapsulated drug after the synergic effect of low pH (4.5), increased concentration of hydrogen peroxide (50 μM), and increased temperature due to the applied magnetic field. In addition, these nanovectors presented excellent specific absorption rate values (up to 1345 W/g) considering the size of the magnetic component, rendering them suitable as potential hyperthermia agents. The presented nanovectors were progressively internalized in U-87 MG cells and in their acidic compartments (*i.e.*, lysosomes and late endosomes) without affecting the viability of the cells, and their ability to cross the blood-brain barrier was preliminary investigated by using an *in vitro* brain endothelial cell-based model. When stimulated with alternating magnetic fields (20 mT, 750 KHz), the nanovectors demonstrated their ability to induce mild hyperthermia (43°C) and strong anticancer effects against U-87 MG cells (scarce survival of cells characterized by low proliferation rate and high apoptosis levels). The optimal anticancer effects resulted from the synergic combination of hyperthermia chronic stimulation with the controlled temozolomide release, highlighting therefore the potential of the proposed drug-loaded lipid magnetic nanovectors for the treatment of glioblastoma multiforme.

Keywords: glioblastoma multiforme; magnetic hyperthermia; lipid nanovectors, temozolomide; apoptosis.

View Article Online
DOI: 10.1039/C8NR05520C

Introduction

Glioblastoma multiforme (GBM) is one of the most malignant brain tumors associated with high percentages of mortality worldwide and with a 5-year survival rate of less than 10%. [1] The inability to treat this form of cancer lies to several factors, including its rapid growth, the location and the pathophysiology of the tumor that in many cases forbid its surgical resection, and the blood-brain barrier (BBB) that hinders the efficient delivery of various chemotherapeutics to the malignant tissue. [1-3]

The contemporary approaches for the treatment of GBM consist of surgical resection, radiotherapy (the role of which is controversial), adjuvant or neoadjuvant chemotherapy using temozolomide, and, finally, hyperthermia using superparamagnetic iron oxide nanoparticles [4, 5]. Although in certain cases the median overall survival of patients increases, in the majority of the patients these treatments have a more palliative than curative role.

The combination of surgical resection and chemotherapy is used as a gold standard for many forms of cancer (*e.g.*, breast, prostate, pancreatic, *etc.*), but, unfortunately, not all the patients are able to undergo this combinatory therapy, leading to an unmet clinical need. In addition, in many cases where the patient can undergo this combinatory treatment, the side-effects from the administered chemotherapeutics negatively affect the quality of life of the patient resulting into a controversy concerning their use. Radiotherapy is another form of treatment which is also used in combination with chemotherapy, in cases where surgery cannot be performed, but this combination not only is less effective than chemotherapy and surgery, but it also results into an increased number of side effects causing the same controversies as chemotherapy.

One of the reasons of the low success rates in increasing the patient survival stems from the low efficacy of the used chemotherapeutics due to various reasons, including the fast reticuloendothelial system clearance, the non-controllable bio-distribution, and the inability to cross the BBB. [1, 6, 7]

In order to overcome the limitations that the current chemotherapeutics like temozolomide (TMZ) present, these chemical substances are encapsulated inside delivery vehicles aiming at improving their efficacy. These delivery vehicles are made of a variety of different materials like synthetic and/or natural polymers and lipids, and can be in the form of microspheres, nanospheres, nanoparticles, micelles, nanorods, nanotubes, hydrogels, and others. [8-12] Each

View Article Online
DOI: 10.1039/C8NR05520C

one of these systems present their own advantages and disadvantages and depending the application, a different type is used every time.

These vectors can be also designed in a way to alter their physicochemical properties under a specific stimulus, which can be physical, chemical, biological, or any combination of them. This ability enhances the efficacy of the synthesized vehicles, since by controlling their properties, drug release, increase of temperature, or their guidance in the cancerous tissue can be achieved in a controlled manner. [8, 11, 13]

These delivery vehicles (or nanovectors), demonstrate a biomimetic character with increased biocompatibility and low immunogenicity which allows them, as mentioned above, to effectively deliver in a controlled way various therapeutic substances. Their small size and their ability to be coated with a variety of natural or synthetic materials allow them to increase their circulation time in the blood, and to effectively deliver the encapsulated therapeutic molecules towards the tissue of interest. Because of the difficulty that the majority of the used therapeutic agents face in crossing the BBB, a limited number of nanovectors can be used for the treatment of GBM and these nanovectors are comprised of various lipids that can be classified in different types, the most common of which include solid lipid nanoparticles (SLNs), nanostructured lipid carriers (NLCs), and liposomes (LS). [14] These nanovectors present an inherent ability to cross the BBB and when properly functionalized demonstrate an enhanced targeting ability and a subsequent increased uptake by the endothelial cells of the BBB, as well as by glioblastoma cells like the U-87 and U-251 malignant glioma (MG) cells.

During the last few years, and especially after that the food and drug administration (FDA) approved the use of superparamagnetic iron oxide nanoparticles (SPIONs) as magnetic resonance imaging contrast agents as well as for the treatment of brain cancer using hyperthermia, many researchers presented studies where lipid-based delivery vehicles encapsulating magnetite nanoparticles (Fe_3O_4) and/or chemotherapeutic agents were used for the treatment of this and other types of cancer. [11, 15-17]

During hyperthermia, inorganic nanoparticles like magnetite or maghemite (γ-Fe_2O_3), coated with synthetic materials like polymers or with natural-derived materials like collagen, albumin, lipids and others, are subjected into an alternating magnetic field (AMF) of specific frequency, that forces them to increase the temperature of their surround environment due to dissipative losses (Néelian, Brownian, and hysteresis).[18]

View Article Online
DOI: 10.1039/C8NR05520C

It has to be noted that, although magnetic hyperthermia is not a novel concept for the treatment of various types of cancer, up to date its use is either experimental or it has been restricted only in patients in a small number of clinical trials, and this is mainly because the use of hyperthermia alone is not enough to cure GBM.

Taking into consideration all the above limitations concerning the use of smart drug delivery systems, we hypothesized that the combination of magnetic hyperthermia, using SPIONs encapsulated in a lipid-based nanovector, with the sustained release of TMZ, a golden standard for GBM, will increase the therapeutic efficacy of the designed nanovector, resulting into increased apoptosis and into the subsequent death of glioblastoma cells. A simple one-pot procedure was used to synthesize the composite nanovectors, which were morphologically, physicochemically, as well as magnetically characterized. The designed lipid-based magnetic nanovectors (LMNVs) demonstrated high stability in water as well as in media that simulated the body fluids, and a sustained release profile for a period of seven days. The LMNVs succeeded in increasing the temperature of the solution from 37°C to 43°C in just a few minutes with better hyperthermia properties (specific absorption rate and intrinsic loss power) than bare SPIONs. Chronic stimulation under an AMF of the U-87 MG cell line, in the presence of just 400 μg/cm^2 of LMNVs, led to an increase in apoptosis after 4 days by 30%, and to a reduction of proliferation by 80%.

View Article Online
DOI: 10.1039/C8NR05520C

Results and discussion

Synthesis procedure

The lipid-based magnetic nanovectors presented in this study were fabricated following a combination of a hot ultra-sonication and a high pressure homogenization (HPH) method. Ultra-sonication resulted in the formation of a nano-emulsion which was further homogenized using the HPH. Dynamic light scattering studies on LMNVs fabricated only by the hot ultra-sonication method (results not presented here) demonstrated that the nanovectors had similar hydrodynamic diameter but increased polydispersity, rendering mandatory the use of HPH in order to achieve a monodisperse population. The chosen temperature for the melting and the subsequent homogenization of the lipid mixture was chosen to be 70°C, which is higher than the melting temperature (57-65°C) of the primary lipid (glycerol monostearate, GMS), in order to have a homogeneous dispersion of the secondary lipids as well as of the SPIONs in the main lipid matrix. In addition, this temperature is close to the boiling point of ethanol which is used as a dispersant for the SPIONs, allowing its complete evaporation and the formation of a homogeneous liquid film. The choice of Tween® 80 as a stabilizer was made basing on literature findings were it is demonstrated that Tween® 80 enhances the delivery of nanoparticles across the BBB due to its ability to adsorb a variety of lipoproteins such as apo-lipoprotein A, E, and others [19, 20].

Morphological and physicochemical characterization

The LMNVs were firstly characterized using transmission electron microscopy (TEM) and the results are presented in Figure 1A (and in supplementary information, Figure S1). The LMNVs present a spherical shape and a relatively low polydispersity in the nanometer range. Their size distribution after analysis with Image J (see supplementary information, Figure S1C) shows that 86% of the nanovectors have a size less than 50 nm with only a small number of them exceeding the 100 nm. These results are in agreement with the dynamic light scattering as well as with the nanoparticle tracking analysis (NTA) data that are presented below. The magnified image of the unstained LMNV presented in Figure 1A2 demonstrates the homogeneous dispersion of the SPIONs inside the lipid matrix of the nanovectors, which is also proved by the electron dispersive X-ray (EDS) mapping of iron (Fe) and oxygen (O) in Figure 1A3 and Figure 1A4, respectively. In order to quantify the amount of each element in the fabricated LMNVs, we performed an EDS analysis (Figure S2) and we calculated the percentage per weight of each element. The results demonstrate the presence of C (24.6 %),

View Article Online
DOI: 10.1039/C8NR05520C

O (35.13 %), and Fe (40.14 %) proving the existence of a lipid as well as an iron-based component.

The surface of LMNVs was characterized using X-ray photoelectron spectroscopy (XPS) (Figure 1B) from which it was found that the percentage of Fe on their surface comprises the 0.8% of the surface elements (C: 81.6%, O: 15%, N: 0.6%, Na: 1.0, Cl: 0.2%, Si: 0.7%). Analysis of the binding energy region between 700 eV and 740 eV, typical of Fe 2p peaks, revealed the presence of Fe $2p_{3/2}$ and Fe $2p_{1/2}$ peaks at approximatively 710.4 eV and 724.1 eV, respectively; importantly, the collected data do not show the presence of any well-defined satellite peak in the region between the two XPS peaks. The observed positions, together with the absence of the satellite peak, are in good agreement with results reported in a previous study [21] on Fe_3O_4.

Infra-red spectroscopy was also used as a complementary technique to verify the presence of SPIONs inside the LMNVs. The spectra of the SPIONs as well as of the LMNVs are presented in Figure 1C. The peaks in the range of 550-600 cm^{-1} that are visible both in the spectrum of SPIONs (bottom) and of LMNVs (top) can be attributed to the vibrations between Fe-O of the encapsulated SPIONs. The peaks at 1100 cm^{-1} and at 1730 cm^{-1} that can be seen only in the LMNVs spectrum (Figure 1C - top) are attributed respectively to the C-O and C=O stretching vibrations of the aliphatic chain of the lipids. The peaks at 2841 cm^{-1} and 2914 cm^{-1} in the LMNVs spectrum belong to the C-H stretching vibrations of the aliphatic chain, while the broad peaks in the range of 3100-3500 cm^{-1}, that can be seen in both spectra, are attributed to O-H stretching vibrations. These results support the presence of SPIONs inside the lipid matrix.

The total percentage of Fe inside the LMNVs as well as the amount of SPIONs inside the LMNVs was calculated using inductively coupled plasma optical emission spectroscopy (ICP-OES) and thermogravimetric analysis (TGA), respectively. ICP-OES results showed that Fe represents 66.8% of the LMNVs, while the thermogravimetric analysis demonstrated that 88% of the LMNVs is comprised of SPIONs. Thermogravimetric analysis on the LMNVs was carried out in order to calculate the percentage of encapsulated SPIONs, as well as to evaluate any structural changes related to temperature alterations. Figure 1D depicts both the weight loss and the differential thermogravimetric curve of the LMNVs. From these curves it is evident the structural deformation as well as the decomposition of the lipid and of the polymeric part of the nanostructure. When temperature is above 50°C a weight loss

View Article Online
DOI: 10.1039/C8NR05520C

can be observed which can be attributed to water molecules trapped on the surface of the LMNVs (50-100°C), as well as due to the decomposition of the GMS, mPEG-DSPE (methoxy-poly(ethylene glycol)-1,2-distearoyl-*sn*-glycero-3-phospho-ethanolamine), and DPPC (1,2-dipalmitoyl-rac-glycero-3-phosphocholine). This loss is achieved in multiple steps as it can be observed from the differential thermal analysis graph, where three peaks are presented (Figure 1D). The first peak can be attributed to the degradation of the poly(ethylene glycol) chain derived from mPEG-DSPE, while the second can be attributed to the release of energy due to the structural deformation resulting from the parallel decomposition of all the lipid components. Finally, the third peak can be attributed to the degradation of GMS. Above 380°C, it can be observed that there is no further weight loss due to the fact that both the polymeric and the lipid coating have been completely degraded. The remaining weight can be attributed to the encapsulated SPIONs and corresponds approximately to the 88% of the initial weight as was mentioned before.

Stability studies

The stability of the LMNVs was studied in media with different conductivities and ionic strength, and at different temperatures, in order to assess their behavior in conditions that simulate the cancerous environment, as well as conditions that simulate their exposure to hyperthermia treatment (T > 42°C). In addition, the stability of the LMNVs in relation to the protein corona formation was also assessed by studying their behavior in Dulbecco's modified eagle medium (DMEM) supplemented with 10% fetal bovine serum (FBS).

The results presented in Figure 1E demonstrate that the LMNVs are stable as temperature increases from 25°C to 46°C maintaining an average hydrodynamic diameter (R_d) of 106.2 ± 13.0 nm and a polydispersity index (PDI) of 0.206 ± 0.030. The correlograms presented in Figure 1F demonstrate a good decay time and a flat line at the end of the curves for all the samples, proving the absence of sedimentation over time and over temperature increment, as well as the absence of aggregation. The average Z-potential value of the LMNVs, in various temperatures (Figure 1G), was found to be -19.0 ± 1.3 mV. Although this value is higher than -30 mV which is considered the threshold for the colloidal stability of a system, our fabricated nanovectors demonstrated excellent stability, both in water and in biologically simulated fluids (DMEM+10%FBS). This behavior can be attributed to the synergic effect of the electrostatic repulsion due to the negative surface charge of the LMNVs, as well as the steric hindrances due to the incorporated PEG.

View Article Online
DOI: 10.1039/C8NR05520C

The hydrodynamic diameter values in dynamic light scattering (DLS) are higher compared to the diameters presented in TEM, and this difference can be attributed to the PEG segment that creates a layer around the particles which swells when inside the liquid dispersant, resulting into increased values of the hydrodynamic diameter.

After assessing the stability of the LMNVs at different temperatures, we studied their behavior in different dispersants which more accurately simulate the conditions inside the human body (see supplementary information, Figure S3). Water was used as a control since in our previous measurements it was used to prove the temperature-dependent stability of the LMNVs. The other two dispersants that were used were DMEM and DMEM supplemented with 10% FBS (DMEM+10%FBS). The hydrodynamic diameter graphs (see supplementary information, Figure S3 - top), and the correlograms (see supplementary information, Figure S3 – Bottom) show that the LMNVs are stable in water after 1, 6 and 24 h at 37°C, further proving their stability for longer period than 6 h. In these graphs it can also be observed a significant difference between LMNVs in DMEM and LMNVs in DMEM+10%FBS, a difference that can be attributed to the protein corona formation around the LMNVs, mostly due to the albumin inside the serum. The protein corona is evident at all the time points, since the size distribution of the nanovectors in the DMEM+10%FBS (blue curves) is always shifted on the right (higher hydrodynamic diameters) compared to the LMNVs dispersed in ultrapure water (black curves). This difference between DMEM+10%FBS and water is not evident from the corresponding correlograms, but the difference between these dispersants and the plain DMEM is pretty clear. Plain DMEM graphs present always higher values of hydrodynamic diameter, and this is because the high ionic strength of the media results into aggregates as it can be seen from the graphs in supplementary information, Figure S3, where the curves belonging to the LMNVs dispersed in DMEM (red curves) are shifted into higher hydrodynamic values and present higher intensity. This higher intensity can also be observed in the curves belonging to the LMNVs dispersed in water after 6 and 24 h, suggesting that an aggregation may occur.

In order to further assess the stability of the nanovectors and to assess the probable creation of aggregates in water as well as in DMEM and DMEM+10%FBS, we performed nanoparticle tracking analysis (NTA) in all of the dispersants after 24 h. Using this method we were able to assess the behavior of the nanovectors in a liquid under flow, observing each particle separately, since NTA has the ability to record the movement of each dispersed

View Article Online
DOI: 10.1039/C8NR05520C

particle passing through a high resolution camera with a specific speed. The results that are presented in supplementary information, Figure S4 and Table S1, demonstrate that there is an aggregation of the LMNVs in water after 24 h (see supplementary information, Figure S4 - black curve, and Table S1 - D50 and D90 values) which cannot be seen in the DLS graphs due to the limitations of the equipment. From Figure S4 and Table S1 it can also be seen that the LMNVs in DMEM and DMEM+10%FBS have lower hydrodynamic diameters compared to water, suggesting firstly that DMEM is not significantly affecting the hydrodynamic values as noticed by the DLS analysis, probably due to the fact that the measurement takes place under flow, and secondly that the LMNVs in DMEM+10%FBS demonstrate good hydrodynamic values that can be attributed probably to the stability that the protein corona offers to the nanovectors. From these studies it can be concluded that the LMNVs present a higher stability in high ionic strength media when these media are supplemented with proteins like those present in the FBS. Although the high ionic strength destroys the Stern layer of the nanovectors in the medium, these nanovectors remain stable probably due to the electrostatic and/or steric interactions between the protein layers. [22-24]

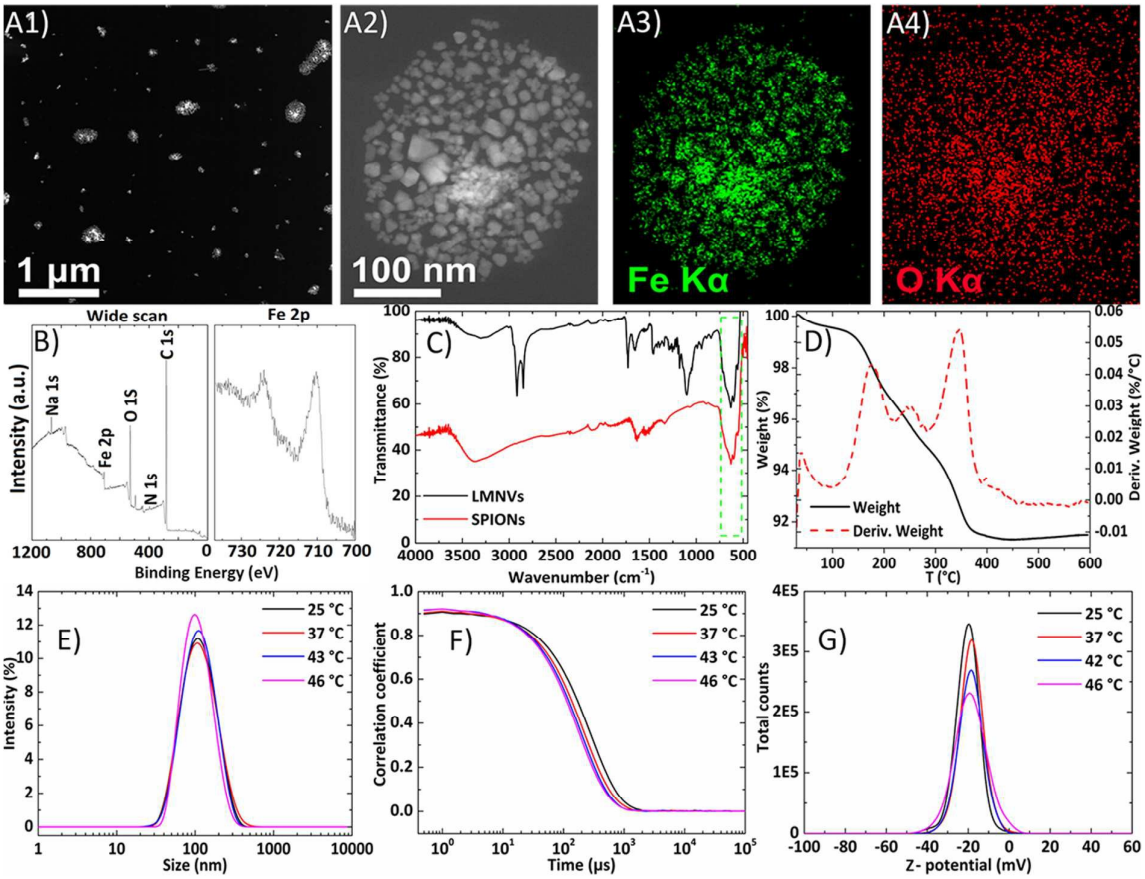

View Article Online
DOI: 10.1039/C8NR05520C

Figure 1. Morphological and physicochemical characterization of LMNVs: A1) high-angle annular dark field-scanning transmission electron microscopy (HAADF-STEM) image of LMNVs, A2) magnified HAADF-STEM image of one unstained LMNV where the distribution of the encapsulated SPIONs is presented, A3) and A4) EDS mapping of Fe and O into a single LMNV, respectively; B) XPS graph demonstrating the elements present on the surface of the LMNVs; C) FT-IR spectra of plain SPIONs (bottom) and LMNVs (top) showing peaks attributed to the SPIONs (Fe-O), depicted inside the green rectangular area, and to the lipid components; D) TGA/DTA graph presenting the weight reduction of the LMNVs during the melting of the lipids and of the polymeric components of the LMNVs (black curve). The red dashed line represents the derivative weight in which each peak represents transition temperatures (melting points) attributed to both the lipid matrix and the incorporated PEG; E) Gaussian distributions of the hydrodynamic diameter (100 nm) of the LMNVs at various temperatures; F) correlograms of the LMNVs at various temperatures demonstrating the stability of the LMNVs; G) surface charge (about -19 mV) of the fabricated LMNVs at various temperatures.

Magnetic characterization

The magnetic properties of the 3 nm SPIONs before and after their encapsulation in the lipid matrix were studied using a superconducting quantum interference device (SQUID). Considering the hysteresis loops measured at room temperature (Figure 2A), it is found that the specific magnetization of the free SPIONs (62 emu/g) is almost two times higher than that one of the LMNVs (32 emu/g), and this difference can be attributed to the additional mass of the lipid matrix. However, the analysis of the hysteresis at low fields (Figure 2B) shows that the SPIONs are “magnetically” different with respect to the LMNVs. Free SPIONs have a coercive field of around 10 Oe, while the LMNVs do not present any coercivity (within the limits of precision of the instrument). The absence of coercivity at room temperature is an indication that all the particles inside the lipid matrix are superparamagnetic. However, the presence of a weak coercivity in the SPIONs indicates the presence of a population of blocked particles. In fact the zero-field cooled and field cooled (ZFC-FC) curves of the SPIONs that are presented in Figure 2C not only exhibit a peak at 200 K that could be correlated with the blocking temperature of the main population of superparamagnetic particles, but they are also separated at room temperature, supporting the presence of a population of blocked particles. In first instance, the blocking temperature is correlated with the particle size of the SPIONs [25, 26], here 3 nm. This size is too small to explain the blocking temperature of 200K and even less the presence of blocked nanoparticles at room temperature. In fact, it is more reasonable to consider that the blocking process is correlated to the inter-particle coupling present in the observed aggregates of SPIONs in the pure sample [25, 27, 28]. In the LMNVs these

View Article Online
DOI: 10.1039/C8NR05520C

aggregates of particles were not observed, thus explaining the full superparamagnetic behavior of the particles at room temperature.

In order to assess the ability of the LMNVs to be used in hyperthermia therapy, we studied the increase of temperature in response to an external AMF at various frequencies. The results presented in Figure 2D demonstrate that 5.4 mg/ml (66.8 % of Fe according to ICP results and 4.8 mg/ml of Fe_3O_4 according to TGA) of LMNVs can increase the temperature of the dispersant from 27.5°C to 46.0°C in 30 min, while the increase from 37.0°C (human body temperature) to 43.0°C (mild hyperthermia temperature) can be achieved in a period of approximately 10 min, demonstrating their potential for *in vitro* and *in vivo* use. Data for stimulation by using 2.4 mg/ml of LMNVs are moreover provided in supplementary information (Figure S5).

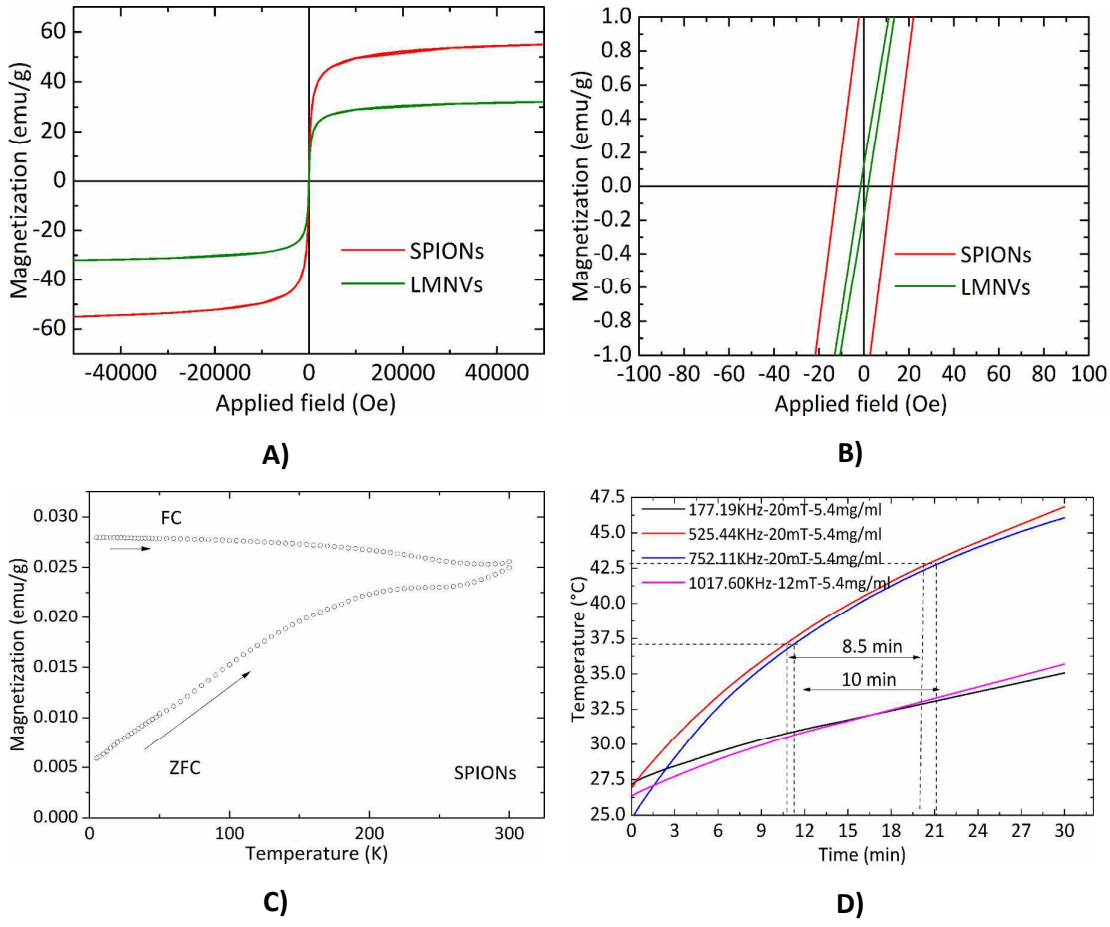

Figure 2. Magnetic characterization: A) magnetization curves of plain SPIONs (red curve) and of LMNVs (green curve) where the saturation magnetization can be seen. These curves indicate the superparamagnetic behavior of the LMNVs; B) magnified images of the hysteresis loops at low magnetic fields where the coercive field is evident and which proves a better superparamagnetic behavior of the LMNVs, since the coercive field of

View Article Online
DOI: 10.1039/C8NR05520C

LMNVs is lower than that one of the 3 nm SPIONs; C) ZFC-FC curves of the plain SPIONs, where it is evident that the plain SPIONs do not fully express their superparamagnetic behavior at room temperature, since the two curves are separated at 300 K; D) response of the LMNVs to an external AMF using various frequencies and magnetic fields for a concentration of 5.4 mg/ml. From this graph it is evident that at frequencies between 525 and 752 KHz it is possible to reach the temperature of 43°C, and that this temperature can be reached in 8.5 min when specific frequencies are used.

The effectiveness for the radiofrequency magnetic hyperthermia is quantified by measuring the specific absorption rate (SAR) and the intrinsic loss power (ILP). In both cases the nanoparticles dispersed in the solvent media are exposed to magnetic fields of different intensities as well as of different frequencies. The increase in the first moments of the irradiation allows the determination of the SAR and ILP, while the highest temperature is given at least after 30 min when an equilibrium is reached. The values presented in Table S2 in supplementary information demonstrate that the used LMNVs are superior to their corresponding controls, which are the plain SPIONs (SAR_{LMNVs} = 1345 W/g *vs.* SAR_{SPIONs} = 678 W/g at 525 KHz and 20 mT, and SAR_{LMNVs} = 1282 W/g *vs.* SAR_{SPIONs} = 611 W/g at 750 KHz and 20 mT). The relation between magnetic hyperthermia and inter-particle interactions / particle aggregation is subject of debate, given the contrasting results found in the literature. [29-32] The samples here investigated are composed by very small magnetic nanoparticles, 3 nm, and the increased SAR values that the LMNVs present can be attributed to the fact that these nanoparticles are more stable (as it was demonstrated by the dynamic light scattering studies) and do not aggregate, as well as to the fact that probably the SPIONs inside the lipid-based matrix act as a single structure, resulting into a synergic effect that enhances SAR. It has to be noted that the SAR values presented in this paper are higher to other studies presented in literature, [33, 34] taking into consideration the experimental conditions. In addition, it should be emphasized the fact that the fabricated LMNVs have the ability to increase apoptosis by 50% under specific treatment, as showed later, and this can be possibly attributed to the fact that the LMNVs generate a localized intracellular hyperthermia that results into cell death through apoptotic mechanisms, as also reported by other groups. [35-38] The ILP values were calculated and reported in Table S2 in order to make easier the comparison among our system and other systems in the literature that use different equipment and measures of the effectiveness of their magnetic-based structures.

Loading and release studies

View Article Online
DOI: 10.1039/C8NR05520C

The percentage of the loaded TMZ (%DL) was found to be 4.1 ± 0.5% (w/w), and was calculated after the extraction of the drug from the nanovectors using the procedure described in the materials and methods. After calculating the dynamic loading, we calculated the encapsulation efficiency, %EE = (weight of the encapsulated TMZ / total weight of TMZ added) x100, as well as the yield, %Y = Total weight of LMNVs / (total weight of lipids + Fe_3O_4 nanoparticles + TMZ), of the loaded nanovectors, and these percentages were respectively 9.9 ± 2.4% and 17.5 ± 1.0%, percentages which are relatively high compared to similar nanoparticles in the literature.[39, 40]

Moreover, it has to be noted that the LMNVs presented a pH and an H_2O_2-dependent release, as well as an enhanced sensitivity to temperature after their exposure to the AMF. The tested pH, 7.4 and 4.5, were used to simulate normal conditions inside the human body as well as the low pH inside the lysosomes. With the same rationale, 50 µM of H_2O_2 was used in order to simulate the overexpressed amount of reactive oxygen species (ROS) in the cancerous cells. The data presented in Figure 3A and Figure 3B demonstrate that the LMNVs present a slow and sustained release of TMZ at physiological conditions (3.3% after 7 days at pH 7.4, black square in Figure 3A), and a slight increase in the release when pH reduces to 4.5 (8.2% after 7 days, black square in Figure 3B). When H_2O_2 is added to the system the release of TMZ does not significantly change with respect to the samples that were not treated with H_2O_2, resulting after 7 days into a release of 1.8% at pH 7.4 and of 5.0% at pH 4.5, respectively (red circles). These release percentages are lower with respect to the corresponding samples at pH 7.4 (3.3%, black square in Figure 3A) and 4.5 (8.2%, black square in Figure 3B) after 7 days, but this decrement cannot be considered significant, since only a difference of 2.8% after 7 days is observed between the samples treated at pH 4.5 (8.2%) and at pH 4.5 + H_2O_2 50 µM (5.4%), while a difference of 1.9% was found between the samples at pH 7.4 (3.3%) and at pH 7.4 + H_2O_2 50 µM (1.4%). On the other hand, when the samples are exposed to magnetic hyperthermia an increased release that reaches 65.8% at pH 7.4 and 63.3% at pH 4.5 can be observed after 7 days. Even after 4 h, the samples that were exposed to hyperthermia released the majority of their cargo (61.0% for pH 7.4 and 57.6% for pH 4.5) demonstrating the immediate effect of the hyperthermia treatment. It seems that the increase in temperature affects the release of TMZ, and this can be attributed to a possible structural deformation of the lipid matrix when the samples are exposed more than one time to the AMF. This structural deformation can also be affected by

View Article Online
DOI: 10.1039/C8NR05520C

the pH as well as by the H_2O_2 that can lead to lipid peroxidation and degradation of the nanovector. Altogether, it has to be noted that when these three factors (temperature, pH and H_2O_2) concur, a synergic effect that results into the complete release of TMZ (100%) after 7 days (Figure 3B), probably due to the complete degradation of the LMNVs, can be observed. On the other hand, when H_2O_2 and hyperthermia are applied at pH 7.4 (Figure 3A), the release (61.3%) after 7 days is not complete. These results suggest that the fabricated LMNVs are excellent delivery vehicles that will allow the release of the encapsulated therapeutics only when a combination of conditions that can be found only in cancerous environments will be applied.

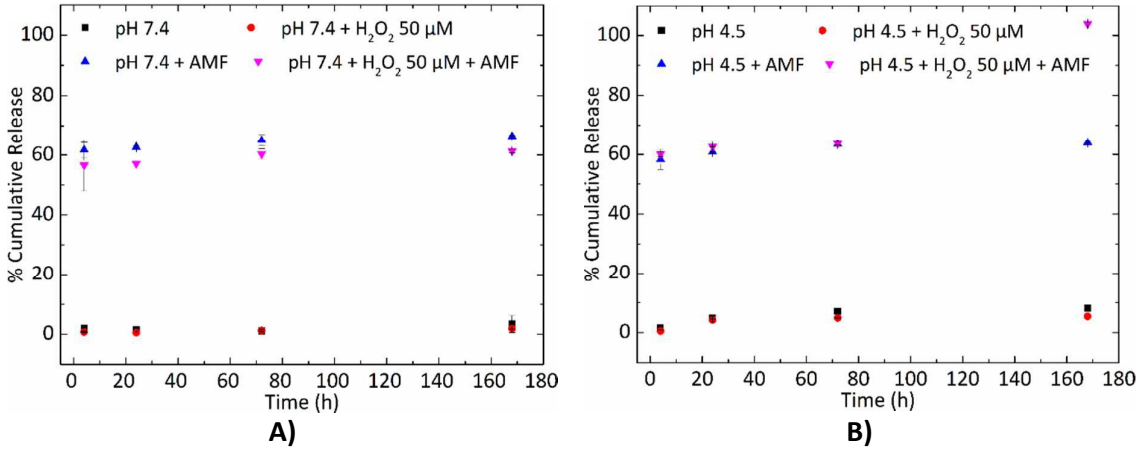

Figure 3. Release profile of TMZ at various time points (4, 24, 72, and 168 h) and under various treatments at A) pH 7.4 and at B) pH 4.5. The presented values are given as mean ± standard error of 3 different measurements. LMNVs present a controlled and sustained release profile when pH is 7.4 and 4.5, while their release profile changes when hyperthermia is applied. The combination of pH and H_2O_2, that is used to simulate the conditions of ROS excess in cancer cells, does not significantly affect the release of TMZ, but the combination of low pH, that can be found in lysosomes (4.5), increased H_2O_2 concentration, and hyperthermia leads to a 100% release, demonstrating the stimuli-responsive nature of the LMNVs.

Internalization studies

The amount of superparamagnetic nanoparticles associated to cells and their specific localization at subcellular level (internalized into different cell organelles or interfaced to plasma membrane) affect the efficiency and the apoptotic/necrotic pathways related to the magnetothermal stimulation. As an example, magnetothermal heating of lysosomes induces an increase of the lysosomal ROS and causes caspase-1 dependent cell death.[35] The nanoparticle-mediated heating of plasma membrane is also able to induce apoptosis by

View Article Online
DOI: 10.1039/C8NR05520C

acting at membrane rafts, activating the damage-associated molecular pattern (DAMP) and subsequently inducing immunogenic cell death (ICD).[41]

For this reason, before performing magnetothermal stimulation, a detailed investigation on the progressive cell up-take of LMNVs, their association to plasma membranes, and their internalization in acidic organelles was carried out (Figure 4). Figure 4A shows confocal laser scanning microscopy (CLSM) imaging of LMNVs (in red), U-87 MG cell membranes (in green), and nuclei (in blue). Qualitatively, an increase of LMNV signal was detected at 72 h of nanoparticle incubation with respect to the 4 h and 24 h time points. Interestingly, the subcellular localization of LMNVs internalized in cells was mostly observed in the cortical region of the cells in proximity of the intracellular side of the plasma membrane, while only a low amount was found in the perinuclear region, most probably because of their lipophilic nature.[42] The CLSM imaging of LMNVs that is presented in Figure 4B (LMNVs in red, acidic organelles in green, nuclei in blue) shows a scarce level of nanomaterial internalization in the acidic compartments at all the different time points (4, 24, and 72 h). However, an increased signal co-localization between LMNVs and acidic organelles was found at 24 h and 72 h of incubation. The increased LMNV internalization during nanoparticle incubation was also confirmed by flow cytometry (Figure S6). Indeed, a progressively enhanced fluorescence emission of cells incubated for 0 h ($2.1 \cdot 10^4 \pm 0.2 \cdot 10^3$ a.u.), 4 h ($16.9 \cdot 10^4 \pm 2.9 \cdot 10^3$ a.u.), 24 h ($60.8 \cdot 10^4 \pm 10.3 \cdot 10^3$ a.u.), and 72 h ($77.6 \cdot 10^4 \pm 9.8 \cdot 10^3$ a.u.) with DiO-stained LMNVs was observed.

View Article Online
DOI: 10.1039/C8NR05520C

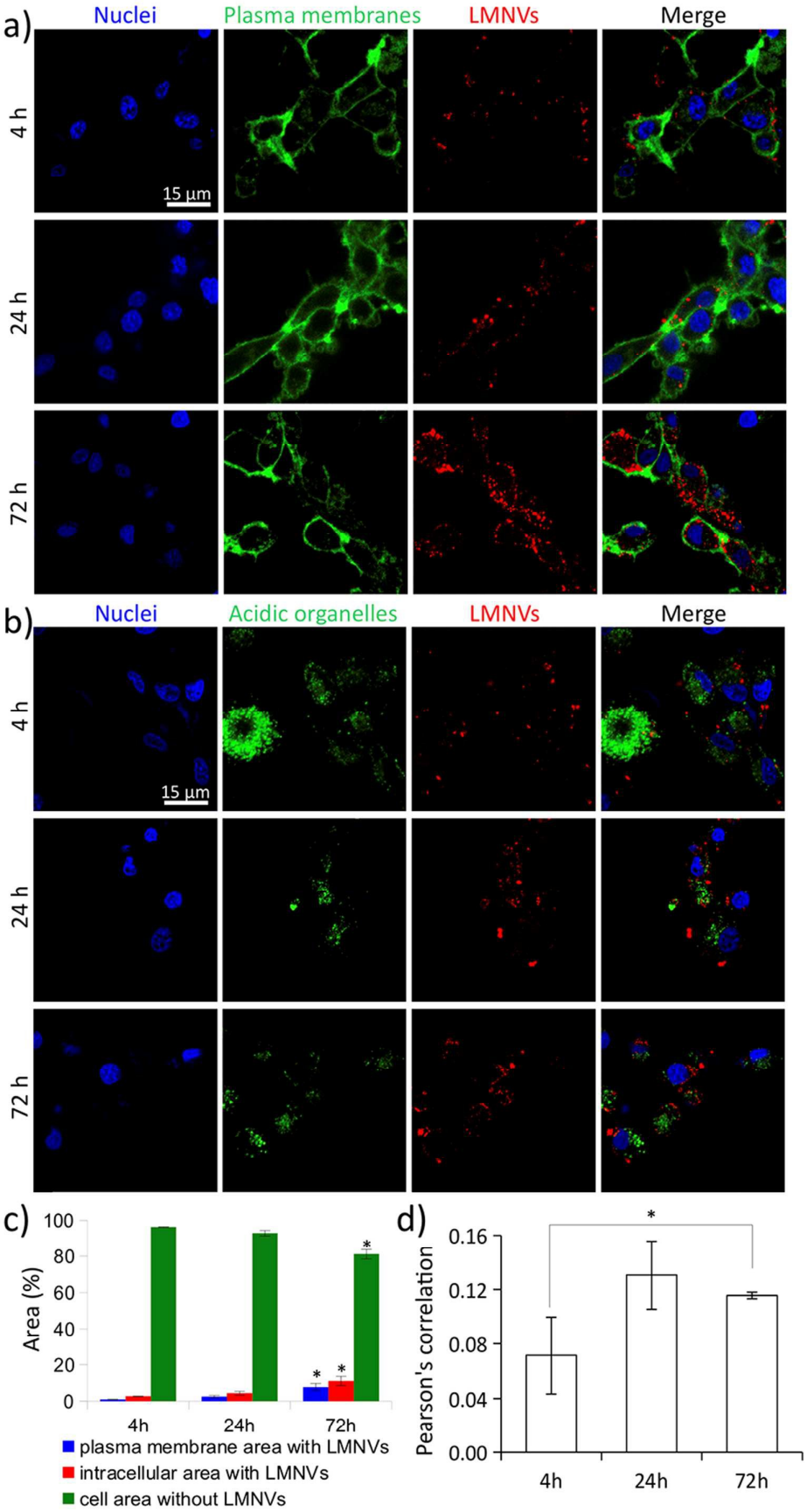

View Article Online
DOI: 10.1039/C8NR05520C

Figure 4. Investigation of the progressive LMNV uptake by U-87 MG cells: nanovector association to plasma membranes and internalization in acidic organelles at 4, 24 and 72 h of treatment. A) Confocal laser scanning microscopy (CLSM) imaging of LMNVs (in red), U-87 MG cell membranes (in green), and nuclei (in blue); B) CLSM imaging of LMNVs (in red), acidic organelles (in green), and nuclei (in blue); C) histograms presenting the area (%) of plasma membrane signal co-localizing with LMNVs (in blue), of intracellular region with LMNVs (in red), and of the whole cell (plasma membrane + intracellular region) without LMNVs (in green); D) histogram presenting the Pearson's correlation analysis among the signals of LMNVs and of the acidic organelles. * $p < 0.05$.

The quantitative analysis of LMNV internalization as well as of their co-localization with cell membrane and acidic organelle signals are shown in Figure 4C and Figure 4D, respectively. The histogram in Figure 4C indicates the area (%) of plasma membrane signal co-localizing with the LMNVs (in blue), of the intracellular region with LMNVs (in red), and of the whole cell (plasma membrane + intracellular region) without LMNVs (in green). As expected, at 72 h of incubation, a significant increase of the plasma membrane area (7.8 ± 2.0 %) and of the intracellular region (11.2 ± 2.6 %) containing LMNVs were measured with respect to both 4 h (area of plasma membrane with LMNVs was 1.0 ± 0.1 %; intracellular region with LMNVs was 2.7 ± 0.1 %; $p < 0.05$) and 24 h (area of plasma membrane with LMNVs was 2.6 ± 0.6 %; intracellular region with LMNVs was 4.4 ± 1.0 %; $p < 0.05$) treatments. At the 72 h time point, a relatively large amount of the total cell area (plasma membrane + intracellular region) resulted occupied by LMNVs (19.0 ± 4.5 %), compared to the 4 h (3.7 ± 0.2 %) and to the 24 h (7.0 ± 1.5 %) time points. The histogram presented in Figure 4D shows the Pearson's correlation analysis among the signals of LMNVs and of the acidic organelles. A significant, yet low, increase of signal co-localization was found just at 72 h (0.116 ± 0.003) compared to 4 h (0.071 ± 0.008; $p < 0.05$), thus indicating a progressive slow internalization of LMNVs in acidic compartments. No significant differences were found at the 24 h intermediate time point (0.130 ± 0.025; $p > 0.05$) with respect to the other time points.

Cytotoxicity studies

In order to assess the cytotoxic effect of the fabricated LMNVs, cell proliferation studies using the WST-1 assay were performed. LMNVs, TMZ-LMNVs and free TMZ that corresponds to the amount loaded in the LMNVs were tested at various concentrations (100, 200, 400 and 800 μg/ml for the nanovectors and 2.2, 4.4, 8.75 and 17.5 μg/ml for the free TMZ, respectively) and at two time points (24 and 96 h). The results presented in Figure S7A

View Article Online
DOI: 10.1039/C8NR05520C

demonstrate that for the first 24 h the LMNVs do not induce any toxicity even at concentrations up to 800 μg/ml, while the TMZ-LMNVs cause a reduction of the metabolic activity, compared to the control, at the highest used concentration (800 μg/ml), which nevertheless is not statistically significant. It has to be noted that the corresponding amounts of free TMZ at 24 h, do not induce a reduction in the metabolic activity of the cells, suggesting that the toxicity highlighted in cells after a 24 h treatment with 800 μg/ml of TMZ-LMNVs can be attributed to an enhanced TMZ cellular up-take. After 96 h it is evident that the metabolic activity of cells treated with plain LMNVs is increased compared to the controls, proving the non-toxicity of the fabricated nanovectors. On the other hand, a reduced increase in the metabolic activity at 96 h at 400 and 800 μg/ml is evident for the cells treated with TMZ-LMNVs, and this decrease can be attributed to an enhanced delivery of TMZ inside the cells. A reduced metabolic activity is finally evident in cells treated with free TMZ, proving its anti-proliferative ability, that is enhanced when loaded inside the presented nanovectors as stated above. Cytotoxicity studies were also performed with and without the exposure of free TMZ, LMNVs and TMZ-LMNVs in an alternating magnetic field, and the results are given in the following paragraph.

Chronic AMF stimulation

The effects of the drug-loaded LMNV (TMZ-LMNVs)-assisted magnetothermal treatment were investigated on U-87 MG cells after 4 days of AMF treatment (2 h *per* day) by analyzing the apoptotic levels with flow cytometry analysis following annexin V-FITC/PI staining, the expression of the Ki-67 proliferation nuclear marker, of the p53 tumor suppressor (Figure 5), and of the cell culture metabolism through WST-1 assay (see supplementary information, Figure S7B). Eight different experimental conditions were considered for these experiments: non-treated control cultures exposed or not to AMF (named “Control+AMF” and “Control”, respectively), cultures treated with 8.75 μg/ml TMZ (amount corresponding to 400 μg/ml of TMZ-LMNVs) and exposed or not to AMF (named “TMZ+AMF” and “TMZ”, respectively), LMNV-incubated cultures exposed or not to AMF stimulation (named “LMNVs” and “LMNVs+AMF”, respectively), and finally, TMZ-LMNV-treated cultures exposed or not to AMF stimulation (named “TMZ-LMNVs” and “TMZ-LMNVs+AMF”, respectively). Figure 5A shows the flow cytometer scatter plots (PI *vs.* annexin V-FITC) and representative confocal images of the immunostaining of the p53 expression (in green), and of the Ki-67 expression (in red) for each experimental condition; in all fluorescence images nuclei are counter-

View Article Online
DOI: 10.1039/C8NR05520C

stained in blue. We observed that the chronic AMF stimulation was able to affect the viability and the proliferation levels of U-87 MG cells, just in the presence of LMNVs or TMZ-LMNVs. Indeed, higher annexin V-FITC fluorescence emissions (apoptotic populations are highlighted in magenta) in concomitance with a higher expression of p53 tumor suppressor and lower levels of the Ki-67 proliferation marker were found in both LMNVs+AMF and TMZ-LMNVs+AMF, with respect to the other experimental groups. A higher nuclear expression of p53 (prevalently cytoplasmatic) was detected in both LMNVs+AMF and TMZ-LMNVs+AMF groups compared to the untreated samples, which was followed by a prominent decrease of cell number. No relevant differences were found among Control+AMF and Control groups. This result reveals the safety of the AMF approach contemplated for the local stimulation of LMNVs-treated cancer cells. Qualitatively, a small increase of the annexin V^+ cells and of $p53^+$ nuclei was detected in TMZ-LMNVs compared to the control and to the LMNVs experimental groups, probably due to the non-specific release of TMZ from the drug-loaded vectors. Moreover, a small increase of annexin V^+ cells and of $p53^+$ nuclei was detected in TMZ-LMNVs, TMZ and TMZ+AMF groups compared to the Control and to the LMNVs experimental groups, thus confirming the pro-apoptotic effects of the drug.

Quantitative analyses are provided in Figures 5B and 5C. In Figure 5B the histogram related to the percentage of viable (in black) and annexin V^+ apoptotic (in magenta) cells for each experimental condition is reported. The percentages of the apoptotic cells in the entire population that was treated with LMNVs+AMF (44.5%) and with TMZ-LMNVs+AMF (50.0%) were significantly higher with respect to Control (6.4%), Control+AMF (0.6%), TMZ (9.4%), TMZ+AMF (10.8%), LMNVs (6.6%) and TMZ-LMNVs (9.3%) groups ($p < 0.05$). Single distributions are reported in supplementary information, Figure S8.

The histogram of Figure 5C reports the percentage of proliferative cells (in green) and of quiescent cells (in orange) for each of the six experimental groups, evaluated after the Ki-67 staining. The percentage of the proliferative cells in LMNVs+AMF (22.6 ± 1.0 %) and in TMZ-LMNVs+AMF (18.2 ± 2.4 %) groups are significantly lower with respect to Control (73.8 ± 1.1 %), Control+AMF (71.3 ± 2.2 %), LMNVs (67.9 ± 5.0 %) and TMZ-LMNVs (65.75 ± 1.18 %) groups ($p < 0.05$). The best results in terms of apoptotic and anti-proliferative effects were observed in the TMZ-LMNVs+AMF group, thus highlighting the effectiveness of the synergic treatment by using magnetothermal stimulation and chemotherapy. [34]

View Article Online
DOI: 10.1039/C8NR05520C

Coherently with the lower number of cells revealed in TMZ-LMNVs+AMF and LMNVs+AMF treated cultures, analysis of WST-1 absorbance showed a remarkable ($p < 0.005$) decrease of the cell metabolism in these two experimental conditions (11.4 ± 0.2% for TMZ-LMNVs+AMF; 15.4 ± 0.3% for LMNVs+AMF) compared to all the other experimental groups: Control (100.0 ± 1.9 %), Control+AMF (106.1 ± 0.7 %), LMNVs (104.7 ± 1.8 %), TMZ-LMNVs (62.7 ± 3.1 %). A small, yet significant ($p < 0.05$), decrease could also be observed after 96 h between the untreated samples (Control and the Control+AMF), and the samples treated with temozolomide (TMZ, 82.4 ± 3.4 %, and TMZ+AMF, 78.8 ± 7.9 %), however these values are still significantly higher with respect to those found for the LMNVs+AMF and TMZ-LMNVs+AMF groups, as reported above.

It is important to highlight that the results acquired from cell metabolism tests are in agreement with the apoptotic evaluation, showing better anticancer performances after the TMZ-LMNVs+AMF combined treatment. Furthermore, the cell metabolism analysis in the TMZ-LMNVs samples highlighted a lower metabolic activity compared to Control, Control+AMF, and LMNVs experimental classes, confirming thus the anticancer effect of TMZ in U-87 MG cells. [43]

View Article Online
DOI: 10.1039/C8NR05520C

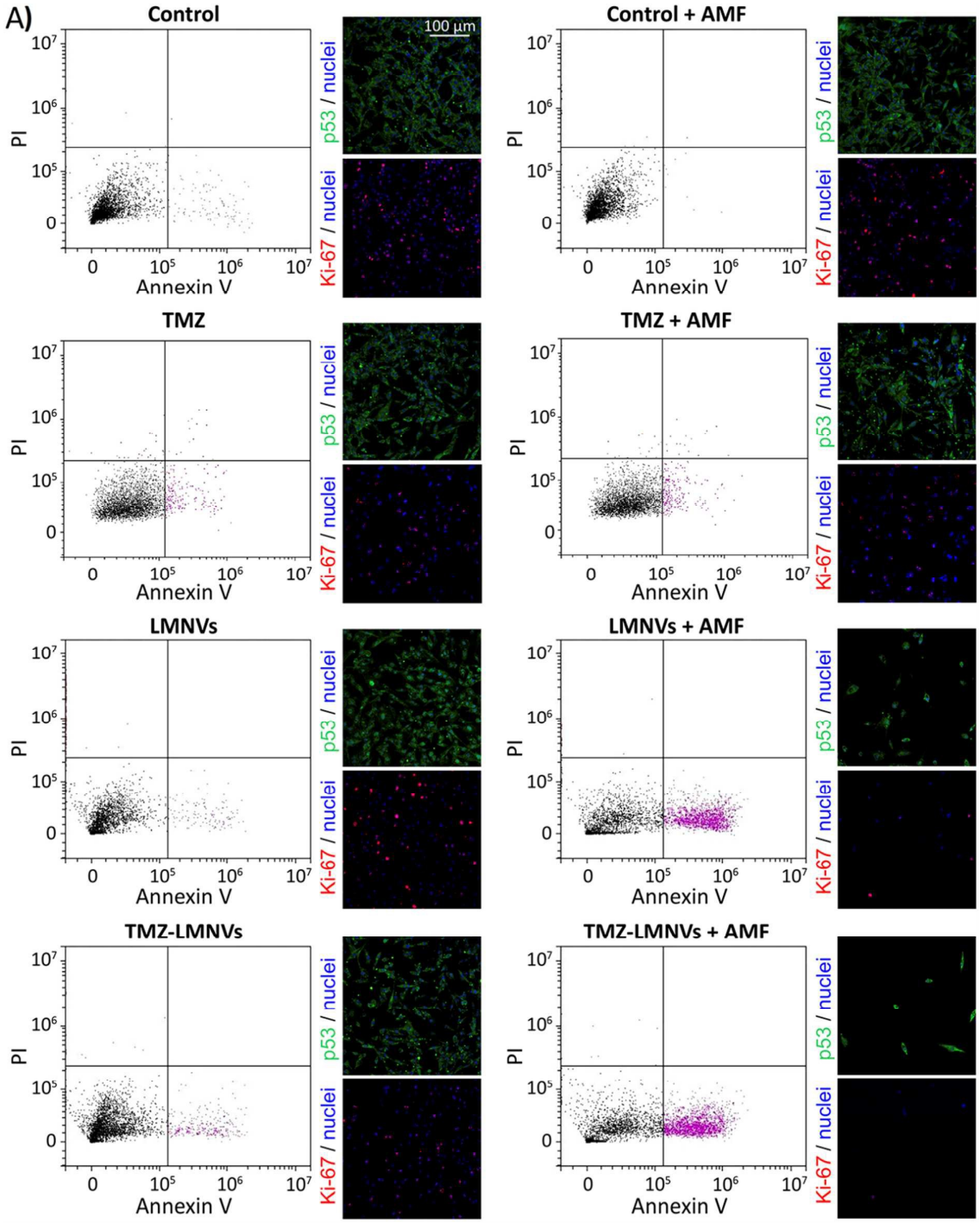

View Article Online
DOI: 10.1039/C8NR05520C

Figure 5. Chronic magnetothermal treatment induces apoptosis, inhibits proliferation, and drastically reduces the U-87 MG cancer cell number. A) Flow cytometer scatter plots (propidium iodide *vs.* annexin V-FITC) and confocal images of p53 expression (in green), Ki-67 expression (in red) and nuclei (in blue) for untreated cells (CTRL), for cells treated with free TMZ, cells treated with plain LMNVs, and cells treated with TMZ loaded LMNVs (TMZ-LMNVs), with (+AMF) and without (-AMF) exposure to an alternating magnetic field. Apoptotic populations in the scatter plots are highlighted in magenta. B) Histograms reporting the percentage of viable (in black) and annexin V^+ apoptotic (in magenta) cells for each experimental condition. C) Histogram presenting the percentage of proliferating cells (in green) and of quiescent cells (in orange) following Ki-67 expression evaluation.

View Article Online
DOI: 10.1039/C8NR05520C

Preliminary analysis of LMNV crossing through an *in vitro* BBB model

The ability of LMNVs to cross an *in vitro* BBB model was preliminary investigated (Figure 6), as previously reported in literature [44]. Briefly, two-compartment BBB models consisting of porous scaffolds (with pores of 3 μm diameter) were used to culture brain endothelial cells (BEC) at high confluence. The developed endothelial layer completely covered the porous scaffold, separating the luminal chamber (on the top) by the abluminal compartment (on the bottom), and was characterized by a sustained expression of the tight junction marker *zonula occludens*-1 (ZO-1; Figure 6A). The BBB model showed a transendothelial electrical resistance (TEER) of 42 Ω·cm^2 and its permeability to 50 μg/ml of FITC-dextran (4 kDa) was significantly lower with respect to the plain porous scaffold (without cells; Figure 6B; $p < 0.05$).

A progressive crossing of DiO-stained LMNVs through the BBB was detected when treating the luminal compartment of the BBB model with 1.3 mg/ml of DiO-stained LMNVs (Figure 6C), with 7.00 ± 1.82 μg, 22.00 ± 1.40 μg and 52.00 ± 8.96 μg crossing to the abluminal compartment at, respectively, 4, 24 and 48 h of incubation. Figure 6D shows the fluorescence emission distributions of U-87 MG cells seeded in the abluminal compartment at 4h, 24 h, and 48 h of incubation with the DiO-stained LMNVs in the luminal chamber. It is possible to appreciate a progressive shift of the distributions to higher values of fluorescence emission by increasing the incubation time: the percentage of LMNV$^+$ cells was 0.5%, 3.3% and 16.5% at, respectively, 4, 24 and 48 h of incubation. Figure 6E shows representative CLSM imaging of U-87 MG cells (f-actin in red, nuclei in blue) in the abluminal compartment after 48 h of incubation with DiO-stained LMNV in the luminal chamber.

These preliminary results concerning the ability of LMNVs to cross the BBB are certainly promising, and pave the way to test the efficiency of the presented nanovectors on more relevant *in vivo* GBM models for preclinical evaluations.

View Article Online
DOI: 10.1039/C8NR05520C

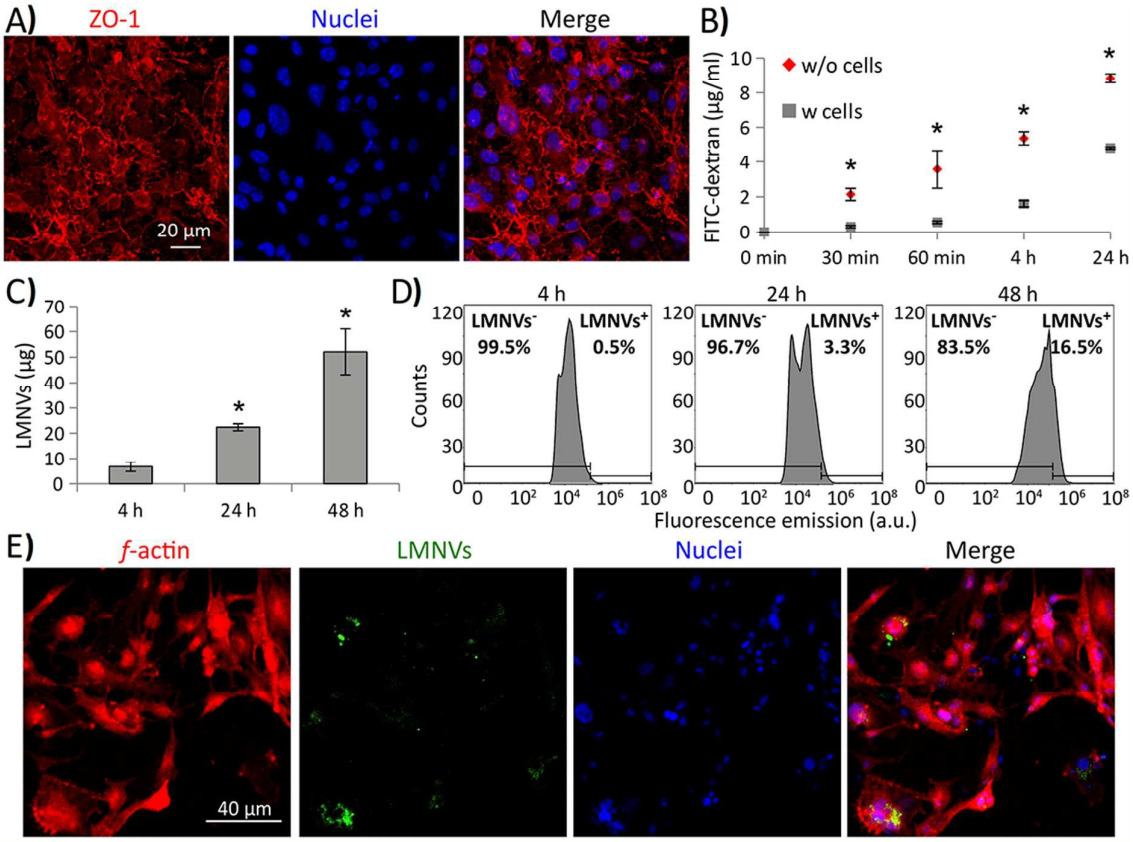

Figure 6. Ability of LMNVs to cross an *in vitro* BBB model. A) Expression of the tight junction marker *zonula occludens*-1 (ZO-1 in red, nuclei in blue); B) crossing of the BBB (with cells; in gray) and of the plain porous scaffold (without cells; in red) of 4 kDa FITC-dextran used as a model substance; C) progressive crossing of DiO-stained LMNVs through the BBB model after treating the luminal compartment with 1.3 mg/ml of DiO-LMNVs; D) fluorescence emission distributions of U-87 MG cells seeded in the abluminal compartment at 4h, 24 h, and 48 h of incubation with DiO-stained LMNVs in the luminal chamber, showing the progressive uptake of the DiO LMNVs by the U-87 MG cells; E) representative CLSM images of U-87 MG cells (f-actin in red, nuclei in blue) in the abluminal compartment after 48 h of incubation with DiO-stained LMNV incubation in the luminal chamber. * $p < 0.05$.

View Article Online
DOI: 10.1039/C8NR05520C

Materials and methods

Preparation of the lipid-based magnetic nanovectors

25 mg of 1-stearoyl-rac-glycerol (Sigma-Aldrich), 2.5 mg of oleic acid (Sigma-Aldrich), 2.5 mg of 1,2-dipalmitoyl-rac-glycero-3-phosphocholine (Sigma-Aldrich), 4 mg of mPEG-DSPE$_{5k}$ (Sigma-Aldrich), and 2.5 mg of temozolomide (Sigma-Aldrich) (when TMZ-LMNVs are fabricated), are mixed with 84.5 µl of an ethanol solution of superparamagnetic iron oxide nanoparticles (15 wt%; US Research Nanomaterials Inc.), inside a 6 ml glass vial. Subsequently, the vial is placed inside an ultrasonic bath (Elmasonic S 35w) set at 70°C in order to melt the lipids and to allow ethanol to evaporate. After ethanol evaporates, 3 ml of a pre-warmed (70°C) Tween® 80 (Sigma-Aldrich) solution (1.0 wt %) are added to the lipid mixture and are immediately sonicated using an ultrasonic homogenizer (Fisherbrand™ Q125 Sonicator) for 15 min (amplitude 30%, 120 W). After the ultrasonic homogenization the hot mixture is transferred to a high pressure homogenizer (HPH, EmulsiFlex-B15 from Avestin) where the sample is further homogenized by passing 5 times through the homogenizer at a pressure of 100000 psi. After the homogenization, the LMNVs are placed for 30 min at 4°C to allow the lipid-based structures to stabilize. The LMNVs are purified by centrifugation and washing with ultrapure (Mili-Q) water (3 times for 30 min at 4°C).

Morphological and physicochemical characterization

Electron microscopy and elemental analysis

The morphological characterization of the microcapsules was performed in high-angle annular dark field-scanning transmission electron microscopy (HAADF-STEM) imaging mode using an image-aberration-corrected TEM JEOL JEM-2200FS, operated at 200 kV. The EDS mapping has been acquired using a Bruker XFlash 5060 silicon-drift detector (SDD), with 60 mm^2 effective area. 20 µl of a concentrated sample were casted on a silicon substrate and dried on air. Afterwards, the dried sample was coated with gold and placed under examination, using a voltage of 20 KeV and a current of 83 pA. The quantification of the elements was performed using Esprit 1.9 software, after excluding the peaks attributed to silicon (Si) and gold (Au).

X-Ray photoelectron spectroscopic analysis

XPS measurements were performed on a Kratos Axis Ultra DLD spectrometer, using a monochromatized Al Kα source operating at 15 kV and 20 mA. Wide scans were acquired at

View Article Online
DOI: 10.1039/C8NR05520C

an analyzer pass energy of 160 eV, while high-resolution narrow scans were performed at a constant pass energy of 10 eV and steps of 0.1 eV. The photoelectrons were detected at a take-off angle ϕ = 0° with respect to the surface normal. The pressure in the analysis chamber was maintained below $7 \cdot 10^{-9}$ Torr for data acquisition. The data were converted to VAMAS format and processed using CasaXPS software, version 2.3.17.

Fourier-transformed infra-red spectroscopy

Attenuated total reflection Fourier-transformed infra-red spectroscopy (ATR-FTIR) was performed using a Shimadzu Miracle 10. Before the measurements, all the samples were freeze-dried and a small amount of each dried sample was placed on the diamond surface of the IR. The number of scans was set to 45, the scanning range was set from 4000 to 400 cm^{-1}, and the resolution step at 4 cm^{-1}. The graphs were plotted using OriginPro software 9.1.

Inductively coupled plasma analysis

The ICP elemental analysis was carried out *via* inductively coupled plasma optical emission spectroscopy (ICP-OES) with an iCAP 6300 DUO ICP-OES spectrometer (Thermo Scientific) operating at RF power of 1150 W, using a flush pump rate at 100 rpm, auxiliary gas at 0.5 l/min and analysis pump rat at 45 rpm. The samples were dissolved overnight in HCl/HNO_3 3:1 (v/v) and diluted with Milli-Q before analysis.

Thermogravimetric analysis (TGA)

TGA was performed on small samples (5 mg) using a Q500 analyzer from TA Instruments. The scans were performed in the range of 30-600°C, using a 10°C/min heating rate. Cooling was achieved by using by using a 50 ml/min nitrogen flow.

Dynamic light scattering

Dynamic light scattering measurements were performed using a Zeta-sizer NanoZS90 of Malvern instruments LTD. The measurements were carried out at various temperatures (25, 37, 42 and 46°C) and in media with different pH, conductivity, and with different supplements (H_2O, DMEM (Sigma-Aldrich), DMEM+10%FBS). For the hydrodynamic diameter measurements the concentration for all the samples was adjusted to 100 µg/ml. The Z-potential measurements were carried out in ultrapure water at pH 5.5 and the conductivity was adjusted in the range of 30-100 µS/cm. The attenuation of the samples during measurement was approximately 9. The surface charge measurements represent the mean ± standard deviation of 3 different measurements with 17 runs for each of them. Before

View Article Online
DOI: 10.1039/C8NR05520C

each measurement, the samples were sonicated for ~10 s using a Bandelin ultrasonic probe at 8 W, to avoid the presence of aggregates during measurements.

Magnetic characterization

The magnetic properties of the plain SPIONs as well as of the LMNVs were measured using a superconducting quantum interference device (SQUID) from Quantum Design. Hysteresis loops were measured from -50 to 50 kOe at 5 K and 300 K upon zero field cooling. The temperature dependence of the magnetization from 5 to 300 K after zero-field cooling (ZFC) and after field cooling (FC) was recorded applying a probe field of 25 Oe to evaluate the superparamagnetic behavior of the nanoparticles.

Magnetic hyperthermia

Magnetic hyperthermia was performed using a MagneTherm™ equipment from NanoTherics. The applied AMF ranged from 12 mT to 20 mT and the frequencies ranged from 177 KHz to 1017 MHz. The samples were place inside a 2 ml Nalgene tube which was inserted inside a polystyrene case in order to reduce thermal fluctuations. The polystyrene case with the sample were placed inside a round coil of 9 mm with 44 turns and the hyperthermia measurements lasted from 30 min to 2 h. For the 2 h time point, the sample was exposed 2 times, 1 h each, with 1 min of pause of the AMF between the two exposures.

Evaluation of the specific absorption rate (SAR) and of the intrinsic loss power (ILP)

SAR and ILP values were calculated for both plain Fe_3O_4 nanoparticles (3 nm) as well as for the LMNVs according to **Equations 1 and 2**. The amount of plain Fe_3O_4 nanoparticles that was used was 5.0 mg, while the amount of the used LMNVs was 5.7 mg (that, according to TGA, corresponds to 5.0 mg of Fe_3O_4). Both samples, after sonication for 5 min using an ultrasonic probe (Fisher scientific, 120 W, 90% amplification), were placed at a final volume of 100 µl inside typical NMR tubes. The tubes were placed exactly in the center of the coil (9 turn, 44 mm), and the temperature was recorded every 1 s using an OSENSA single channel optic fiber. For the calculation of SAR and ILP values the temperature difference that was used was 6°C, and corresponded to the difference between 37°C and 43°C. The equations used for the calculation of the above parameters are given below. For further details see supplementary information, Table S2.

$$SAR = C_p \cdot \frac{D_c}{C_{Fe}} \cdot \frac{dT}{dt} \qquad \textbf{Equation 1}$$

$$ILP = \frac{SAR}{f \cdot H^2} \qquad \textbf{Equation 2}$$

View Article Online
DOI: 10.1039/C8NR05520C

C_p is the specific heat capacity of the sample, which in our case is 4.18 J g^{-1} K^{-1}; D_c is the density of the colloid at 25°C, which is 0.997 g/ml; C_{Fe} is the concentration of the magnetic moiety in the solvent, *dT* is the temperature difference (in K) at the specific measurement time (*dt*); *dt* represents the first 20 s above 37°C, where the difference in temperature is measured; *f* is the frequency of the magnetic field in Hz and *H* is the intensity of the magnetic field in A/m^2.

Loading and release studies

The loading and the release studies were performed using an HPLC Shimadzu LC-20AT similarly to a previous reported study.[45] The chromatographic separation was carried out using a C-18 column (150 mm x 4.6 mm i.d., 5 µm particle size). The mobile phase consisted of methanol (Sigma-Aldrich) and water containing 1% acetic acid of HPLC grade (Sigma-Aldrich) and pumped in isocratic mode (25% MeOH / 70% H_2O) with a flow rate of 0.5 ml/min. The elution of the analyte was monitored at 328 nm. In order to calculate the percentages of the encapsulated TMZ, as well as the percentages of the cumulative release from the LMNVs, a standard curve using various concentrations of TMZ was made. The standard curve was prepared by dissolving 1 mg of TMZ in 1 ml volume of the mobile phase and filtered using a 0.2 µm syringe filter. A concentration range of 0.1-100 µg/ml was prepared upon further serial dilution. To calculate the loading capacity, 0.25 ml of methanol (MeOH) were mixed with 2.4 mg of TMZ-loaded LMNVs and placed under stirring at 70°C for 3 h. After stirring, 0.75 ml of cold de-ionized water were added to the MeOH dispersion and the samples were centrifuged at 15000 rpm for 2 h at 4°C. The supernatant was collected and measured using the conditions above described. For the release studies, at each time point the samples were centrifuged at 15000 rpm for 1 h at 4°C and the supernatant of each treatment solution was removed and replaced with a fresh one. 80 µl of each supernatant were injected to the HPLC and analyzed using the parameters described above. Because the release studies were made in phosphate-buffered saline solution, the standard curve of TMZ was also performed in the same medium. The temozolomide peak was observed at 5.1-5.3 min.

Cell lines

In this study, the glioblastoma multiforme cell line U-87 MG (ATCC® HTB14™) was used. U-87 MG cells were cultured in T75 flasks using high glucose DMEM (Sigma-Aldrich) supplemented with 10% FBS (Gibco), 1% penicillin/streptomycin (Gibco) and 1% L-glutamine (Gibco), and at

View Article Online
DOI: 10.1039/C8NR05520C

normal culture conditions (37°C, 5% CO_2, 100% humidity). For all the experiments the used cells were between passage 10 and passage 20. The medium during culture was changed every two days.

Internalization studies

LMNV internalization in living U-87 MG cells was investigated at different time points (4, 24, and 72 h) through confocal laser scanning microscopy (CLSM) imaging (C2s system, Nikon), as previously described,[46] and by flow cytometry using a Beckman Coulter CytoFLEX. Before incubation, LMNVs were stained with the Vybrant DiD (1,1'-dioctadecyl-3,3,3',3'-tetramethylindodicarbocyanine, 4-chlorobenzene sulfonate salt) (Thermo Fisher) cell-labeling solution for CLSM, and with Vybrant DiO (3-octadecyl-2-[3-(3-octadecyl-2(3H)-benzoxazolylidene)-1-propenyl]-, perchlorate) (Thermo Fisher) for flow cytometry experiments. Briefly, 10 mg of LMNVs were incubated with 5 µl of DiD or DiO for 30 min at room temperature. After the incubation the nanovectors were centrifuged at 15000 rpm for 60 min at 4°C; the precipitate was collected and re-dispersed in distilled sterile water. The procedure was repeated two times.

Spectral imaging of DiD-stained LMNVs was performed through CLSM (see supplementary information, Figure S9); Figure S9A shows CLSM images of a single DiD-stained LMNV at different emission wavelengths and Figure S9B reports the corresponding relative emission spectrum of Figure S9A, where is evident the characteristic peak (λ ~ 670 nm) of the Vybrant DiD lipophilic dye.

In order to investigate the cell up-take of LMNVs and their accumulation inside acidic organelles (*i.e.*, lysosomes and late endosomes), fluorescent staining of the plasma membrane (CellMask Green Plasma Membrane Stain, 1:1000 dilution, Invitrogen), of the acidic cell compartments (Lysotracker acidotropic probe, 75 nM, Invitrogen), and of the cell nuclei (Hoechst 33342, 1 µg/ml, Invitrogen), was carried out in serum-free DMEM at 37°C. Subsequently, the cells were washed twice with phosphate-buffered saline solution (PBS) (Sigma-Aldrich) and then rinsed with phenol red-free complete medium.

Acquisition parameters of scan area, laser power and amplification gain were maintained constant for all the different acquisitions. Finally, images were analyzed by using NIS-Elements software (Nikon) through a semi-automatic approach. Concerning cell uptake, signals of the plasma membranes and of the LMNVs were selected and measured upon intensity thresholding. Intersection between the two signals indicated the area of the LMNVs

View Article Online
DOI: 10.1039/C8NR05520C

associated to the plasma membrane. The intracellular area was defined by selecting the regions of the CLSM image that do not co-localize with the plasma membrane signal and that contain nuclei. Intersection between the areas associated to the intracellular region and to the LMNVs was then obtained. Co-localization analysis between the acidic organelles and the LMNVs was assessed by investigating the Pearson's correlation parameter at the different time points.

Flow cytometry of cells incubated with DiO-stained LMNVs was performed by analyzing the fluorescence emissions (λ_{ex} = 488 nm; 485 nm < λ_{em} < 565 nm) of cells after 0, 4, 24 h and 72 h of nanoparticle treatment. Statistical analysis was performed using ANOVA, followed by HSD test.

Assessment of cell viability/apoptosis and metabolic activity

The apoptotic effects of the LMNV-assisted magnetothermal stimulation was investigated on U-87 MG cells after 4 days of treatment with chronic AMF, using flow cytometry. Samples treated with LMNVs, TMZ-LMNVs, and untreated samples were exposed to AMF (20 mT, 750 KHz) for 2 h *per* day for 4 days. After 72 h the cells were trypsinized and incubated with annexin V-FITC/PI (Thermo Fisher) for cell death assessment by flow cytometry. Before flow cytometry the cells were stained using the following procedure: cells were washed with Dulbecco's phosphate-buffered saline solution (DPBS) without calcium and magnesium and detached using trypsin-EDTA (0.25%, 5 min at 37°C). After a centrifugation step (10 min at 3000 rpm), cells were stained with 2.5 µM of annexin V-FITC and 1 µg/ml of propidium iodide (PI) in annexin V binding buffer (1x) for 15 min at 37°C protected from light. Cells stained with annexin V-FITC/PI were evaluated using a Beckman Coulter CytoFLEX. The percentage of viable and apoptotic populations were analyzed using the CytoFLEX software and subsequently reported on histograms. Untreated cells were used as controls.

Cell metabolism before and after the chronic magnetothermal stimulation was assessed using the WST-1 assay (Sigma-Aldrich) following a standard protocol previously described.[13] Briefly, cells at pre-determined time points were incubated with the WST-1 reagent (1:10 dilution) for 50 minutes at 37°C and 5% CO_2, and then the supernatant absorbance at 450 nm was measured using a Perkin Elmer Victor X3 UV-Vis spectrophotometer. The measured absorbance values were normalized and expressed as % with respect to the controls.

View Article Online
DOI: 10.1039/C8NR05520C

Annexin V-FITC fuorescence emission distributions were statistically compared by Kruskal-Wallis test followed by Nemenyi-Damico-Wolfe-Dunn *post-hoc* test; WST-1 data were analysed using ANOVA followed by HSD test.

Immunofluorescence against p53 and Ki-67 markers

Immunofluorescence staining against the p53 tumor suppressor and the Ki-67 proliferation markers were performed after 4 days of chronic magnetothermal stimulation, similarly as previously described.[47] Briefly, after fixing cultures with 4% paraformaldehyde (PFA) in PBS (4°C, 25 min), cell membranes were permeabilized with 0.1% Triton X-100 (Sigma-Aldrich) in PBS (room temperature, 25 min), and a subsequent blocking step with 10% goat serum in PBS (room temperature, 1 h) was carried out. Cultures were then incubated with primary mouse monoclonal anti-p53 antibody (1:200 dilution, Abcam) or with primary rabbit IgG anti-Ki-67 antibody (1:150 dilution, Millipore) in 10% goat serum (37°C, 45 min), washed 5 times, and finally incubated with a staining solution composed by TRITC-conjugated secondary anti-rabbit antibody (1:200; Millipore) or FITC-conjugated secondary anti-mouse antibody (1:75; Millipore), and by Hoechst 33342 (1 µg/ml, Invitrogen) for nucleus counterstaining.

After washing 3 times cultures with PBS, imaging was performed by using a CLSM system (C2s system, Nikon) as described above. Analysis of Ki-67$^+$ nuclei was carried out with NIS-Elements software (Nikon) by thresholding and selecting the Hoechst and Ki-67 signals by pixel intensity. Statistical analysis on collected data was performed with ANOVA, followed by HSD test.

BBB model characterization and LMNV crossing studies

BBB model was obtained by culturing bEnd.3 cells (ATCC® CRL-2299™), a well-characterized immortalized mouse BEC line, at high confluence (seeding density = $8{\cdot}10^4$ cells/cm^2 cells/cm^2) for 5 days on porous inserts of Transwell® (Corning; average pore diameter of 3 µm) by using the same cell medium adopted for culturing the U-87 MG cells. The developed endothelial layer completely covered the porous scaffold, separating the luminal chamber (on the top) from the abluminal compartment (on the bottom).

Before performing the LMNV crossing tests, the BBB was characterized in terms of TEER (assessed with a Millipore Millicell ERS-2 Volt-Ohmmeter) and permeability to FITC-dextran (Sigma; molecular weight 4 KDa). Specifically, 100 µl of phenol red-free medium containing 50 µg/ml of FITC dextran were added to the luminal compartments of the BBB or of the

View Article Online
DOI: 10.1039/C8NR05520C

inserts without cells (as controls); the abluminal compartments were filled with 600 µl of phenol red-free medium. The fluorescence emission of the medium in the abluminal compartment was measured with a Perkin Elmer Victor X3 UV-Vis spectrofluorometer (λ_{ex} = 488 nm; λ_{em} = 520 nm) at different time points (30 min, 60 min, 4 h, 24 h and 48 h). The values of fluorescence emission were converted and expressed in terms of FITC-dextran concentrations using a calibration curve, and statistically analyzed using ANOVA followed by HSD test.

The expression of ZO-1 marker of thigh junctions was finally verified by immunofluorescence following treatment with a rabbit IgG primary antibody against ZO-1 (Invitrogen; 1:100 dilution in PBS supplemented with 10% goat serum; 3 h at room temperature) and a goat Alexa Fluor 488-IgG anti-rabbit secondary antibody (Invitrogen; 1:200 dilution in PBS supplemented with 10% goat serum; 2 h at room temperature), following the protocols described for Ki-67 and P53 immunostaining. CLSM was performed by using a C2s system (Nikon).

Concerning LMNV crossing tests, U-87 MG cells were cultured in the abluminal compartments and 1.3 mg/ml of DiO-stained nanovectors were incubated in the luminal chamber of the BBB model. At 4, 24 and 48 h of LMNV incubation, the fluorescence emission of the abluminal medium was measured and converted to concentration as described above for the FITC-dextran studies. Moreover, U-87 MG cells were trypsinized, centrifuged (10 min at 3000 rpm), and the pellet resuspended in PBS for flow cytometry analysis (λ_{ex} = 488 nm; 500nm < λ_{em} < 560nm; CytoFLEX, Beckman Coulter). For the CLSM imaging, U-87 MG cells were fixed and treated with TRITC-conjugated phalloidin (100 µM; Millipore) and Hoechst 33342 (1 µg/ml; Invitrogen) for f-actin and nuclei staining, respectively.

View Article Online
DOI: 10.1039/C8NR05520C

Conclusions

In this work, we have synthesized and characterized lipid-based magnetic nanovectors (LMNVs) that can be used for synergic magnetic hyperthermia and chemotherapy against glioblastoma multiforme. The synthesized LMNVs presented excellent good SAR values, and were able to increase the temperature of media from 37°C to 43°C in approximately 10 min even when high volumes (1 ml) of the prepared magnetic fluid were used. In addition, both the LMNVs and the TMZ-LMNVs demonstrated an increase in terms of apoptotic effects on U-87 MG cells, being the TMZ-LMNVs more effective compared to the unloaded LMNVs. These lipid nanovectors presented also a good loading capacity (4.1%) with a sustained release profile which was found to be stimuli-dependent. At physiological conditions the release of TMZ after 7 days was approximately 3.5%, while when low pH, increased H_2O_2, and magnetic hyperthermia were simultaneously applied, a total (100%) release of TMZ was observed. Cell uptake studies showed a progressive internalization of the nanomaterial that was mostly located in the cortical area of the cells, and that was associated to the intracellular side of the plasma membranes with a partial incorporation into acidic organelles (*i.e.*, lysosomes and late endosomes). Finally, chronic AFM treatments of U-87 MG cells incubated with TMZ-loaded LMNVs demonstrated great anticancer performances, both considering their strong apoptotic and anti-proliferative activity, resulting in an impressive reduction of cancer cell population after 4 days of chronic stimulation (2 h *per* day). The strongest anticancer effects were observed by the application of the magnetothermal stimulation in the presence of the drug-loaded LMNVs, resulting into enhanced therapeutic effects with respect to samples treated just with hyperthermia or only with the drug.

The ability of the LMNVs to overcome the BBB limitation were preliminary studied using an *in vitro* BBB model, and the results showed that after 24 h almost 40% of the LMNVs are able to pass and to be thereafter internalized by the glioblastoma cells.

Future works will be devoted to the functionalization of the proposed LMNVs in order to enhance their crossing through the blood-brain barrier and to facilitate their GBM delivery by exploiting dual targeting approaches. Finally, the anticancer efficiency of this multifunctional nanosystem will be tested on *in vivo* GBM models.

View Article Online
DOI: 10.1039/C8NR05520C

Acknowledgements

This project has received funding from the European Research Council (ERC) under the European Union's Horizon 2020 research and innovation program (grant agreement N°709613, SLaMM).

View Article Online
DOI: 10.1039/C8NR05520C

Bibliography

1. S. K. Carlsson, S. P. Brothers and C. Wahlestedt, *EMBO Mol. Med.*, 2014, **6**, 1359-1370.
2. A. Bhowmik, R. Khan and M. K. Ghosh, *Biomed Res. Int.*, 2015, **2015**, 320941.
3. I. G.; and D. E., *J. Med. Life*, 2009, **2**, 386-393.
4. K. Maier-Hauff, F. Ulrich, D. Nestler, H. Niehoff, P. Wust, B. Thiesen, H. Orawa, V. Budach and A. Jordan, *J. Neuro-Oncol.*, 2011, **103**, 317-324.
5. R. A. Revia and M. Zhang, *Materials today*, 2016, **19**, 157-168.
6. R. K. Oberoi, K. E. Parrish, T. T. Sio, R. K. Mittapalli, W. F. Elmquist and J. N. Sarkaria, *Neuro-oncology*, 2016, **18**, 27-36.
7. G. Minniti, R. Muni, G. Lanzetta, P. Marchetti and R. M. Enrici, *Anticancer Res.*, 2009, **29**, 5171-5184.
8. C. Tapeinos, E. K. Efthimiadou, N. Boukos and G. Kordas, *Colloids Surf., B*, 2016, **148**, 95-103.
9. C. Tapeinos, A. Larranaga, J. R. Sarasua and A. Pandit, *Nanomedicine : nanotechnology, biology, and medicine*, 2017.
10. G. G. Genchi, A. Marino, C. Tapeinos and G. Ciofani, *Front. Bioeng. Biotechnol.*, 2017, **5**, 80.
11. A. Grillone, E. R. Riva, A. Mondini, C. Forte, L. Calucci, C. Innocenti, C. de Julian Fernandez, V. Cappello, M. Gemmi, S. Moscato, F. Ronca, R. Sacco, V. Mattoli and G. Ciofani, *Adv. Healthcare Mater.*, 2015, **4**, 1681-1690.
12. C. Tapeinos, M. Battaglini, M. Prato, G. La Rosa, A. Scarpellini and G. Ciofani, *ACS Omega*, 2018, **3**, 8952-8962.
13. A. Marino, S. Arai, Y. Hou, A. Degl'Innocenti, V. Cappello, B. Mazzolai, Y. T. Chang, V. Mattoli, M. Suzuki and G. Ciofani, *ACS nano*, 2017, **11**, 2494-2508.
14. C. Tapeinos, M. Battaglini and G. Ciofani, *J. Controlled Release*, 2017, **264**, 306-332.
15. M. Munoz de Escalona, E. Saez-Fernandez, J. C. Prados, C. Melguizo and J. L. Arias, *Int. J. Pharm.*, 2016, **504**, 11-19.
16. H. Ming-Huang, L. Chung-Yu and S. Yu-Chuan, Magnetic solid lipid nanoparticles as mediators for controlled hyperthermia, Sanya, China, 2008.
17. A. A. Allam, M. E. Sadat, S. J. Potter, D. B. Mast, D. F. Mohamed, F. S. Habib and G. M. Pauletti, *Nanoscale Res. Lett.*, 2013, **8**, 426.
18. C. Tapeinos, in *Smart Nanoparticles for Biomedicine*, ed. G. Ciofani, Elsevier Inc.2018, pp. 131-142.
19. T. M. Goppert and R. H. Muller, *Journal of drug targeting*, 2005, **13**, 179-187.
20. J. Kreuter, D. Shamenkov, V. Petrov, P. Ramge, K. Cychutek, C. Koch-Brandt and R. Alyautdin, *Journal of drug targeting*, 2002, **10**, 317-325.
21. T. Yamashita and P. Hayes, *Applied Surface Science*, 2008, **254**, 2441-2449.
22. T. L. Moore, L. Rodriguez-Lorenzo, V. Hirsch, S. Balog, D. Urban, C. Jud, B. Rothen-Rutishauser, M. Lattuada and A. Petri-Fink, *Chem. Soc. Rev.*, 2015, **44**, 6287-6305.
23. V. Forest and J. Pourchez, *Mater. Sci. Eng., C*, 2017, **70**, 889-896.
24. I. Lynch and K. A. Dawson, *Nano Today*, 2008, **3**, 40-47.
25. S. Bedanta and W. Kleemann, *J. Phys. D: Appl. Phys.*, 2009, **42**, 013001.
26. I. Prigogine and S. A. Rice, *Advances in Chemical Physics*1997.
27. M. Knobel, Nunes, W. C., Socolovsky, L. M., De Biasi, E., Vargas, J. M., & Denardin, J. C., *J. Nanosci. Nanotechnol.*, 2008, **8**, 2836-2857.
28. K. Nadeem, H. Krenn, T. Traussnig, R. Wurschum, D. V. Szabo and I. Letofsky-Papst, *J Magn Magn Mater*, 2011, **323**, 1998-2004.

View Article Online
DOI: 10.1039/C8NR05520C

29. P. Hugounenq, M. Levy, D. Alloyeau, L. Lartigue, E. Dubois, V. Cabuil, C. Ricolleau, S. Roux, C. Wilhelm, F. Gazeau and R. Bazzi, *J. Phys. Chem. C*, 2012, **116**, 15702-15712.
30. E. L. Verde, G. T. Landi, J. A. Gomes, M. H. Sousa and A. F. Bakuzis, *J. App. Physics*, 2012, **111**, 123902.
31. G. T. Landi, *Phys. Rev. B*, 2014, **89**.
32. M. Campanini, R. Ciprian, E. Bedogni, A. Mega, V. Chiesi, F. Casoli, C. de Julian Fernandez, E. Rotunno, F. Rossi, A. Secchi, F. Bigi, G. Salviati, C. Magen, V. Grillo and F. Albertini, *Nanoscale*, 2015, **7**, 7717-7725.
33. C. Blanco-Andujar, D. Ortega, P. Southern, Q. A. Pankhurst and N. T. Thanh, *Nanoscale*, 2015, **7**, 1768-1775.
34. C. A. Quinto, P. Mohindra, S. Tong and G. Bao, *Nanoscale*, 2015, **7**, 12728-12736.
35. P. Clerc, P. Jeanjean, N. Hallali, M. Gougeon, B. Pipy, J. Carrey, D. Fourmy and V. Gigoux, *J. Controlled Release*, 2018, **270**, 120-134.
36. C. Sanchez, D. El Hajj Diab, V. Connord, P. Clerc, E. Meunier, B. Pipy, B. Payre, R. P. Tan, M. Gougeon, J. Carrey, V. Gigoux and D. Fourmy, *ACS nano*, 2014, **8**, 1350-1363.
37. M. Domenech, I. Marrero-Berrios, M. Torres-Lugo and C. Rinaldi, *ACS nano*, 2013, **7**, 5091-5101.
38. M. Creixell, A. C. Bohorquez, M. Torres-Lugo and C. Rinaldi, *ACS nano*, 2011, **5**, 7124-7129.
39. C. Y. Zhuang, N. Li, M. Wang, X. N. Zhang, W. S. Pan, J. J. Peng, Y. S. Pan and X. Tang, *Int. J. Pharm.*, 2010, **394**, 179-185.
40. G. Chen-yu, Y. Chun-fen, L. Qi-lu, T. Qi, X. Yan-wei, L. Wei-na and Z. Guang-xi, *Int. J. Pharm.*, 2012, **430**, 292-298.
41. O. Szasz, G. Andocs, T. Kondo, M. U. Rehman, E. Papp, T. Vancsik and T. Krenacs, *J. Clin. Oncol.*, 2015, **33**, e22176-e22176.
42. K. E. Burns and J. B. Delehanty, *Ther. Delivery*, 2017, **8**, 235-237.
43. S. Y. Lee, *Genes Dis.*, 2016, **3**, 198-210.
44. M. Rehman, A. Madni, D. Shi, A. Ihsan, N. Tahir, K. R. Chang, I. Javed and T. J. Webster, *Nanoscale*, 2017, **9**, 15434-15440.
45. A. Khan, S. S. Imam, M. Aqil, Y. Sultana, A. Ali and K. Khan, *BENI-SEUF Univ. J. Appl. Sci.*, 2016, **5**, 402-408.
46. A. Marino, M. Battaglini, D. De Pasquale, A. Degl'Innocenti and G. Ciofani, *Sci. Rep.*, 2018, **8**, 6257.
47. A. Marino, C. Filippeschi, G. G. Genchi, V. Mattoli, B. Mazzolai and G. Ciofani, *Acta Biomater.*, 2014, **10**, 4304-4313.

View Article Online
DOI: 10.1039/C8NR05520C

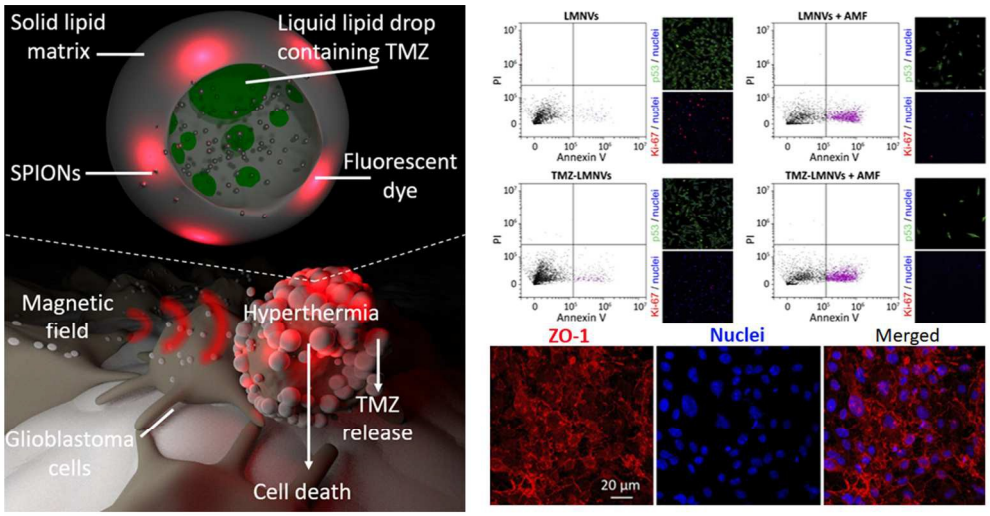

A lipid-based magnetic nanovector loaded with Temozolomide (TMZ), able to cross an *in vitro* BBB model, increases apoptosis in the U87 cell line by the synergic combination of localized intracellular hyperthermia and the controlled release of TMZ, when stimuli including, alternating magnetic field, temperature, pH and increased ROS are combined.